


Hadronic supercriticality in spherically expanding sources: application to GRB prompt emission

Ioulia Florou ¹*, Apostolos Mastichiadis ¹†, Maria Petropoulou ¹‡

¹Department of Physics, National and Kapodistrian University of Athens, University Campus Zografos, GR 15783, Greece

Accepted XXX. Received YYY; in original form ZZZ

ABSTRACT

Relativistic hadronic plasmas can become under certain conditions supercritical, abruptly and efficiently releasing the energy stored in protons through photon outbursts. Past studies have tried to relate the features of such hadronic supercriticalities (HSC) to the phenomenology of Gamma-Ray Burst (GRB) prompt emission. In this work we investigate, for the first time, HSC in adiabatically expanding sources. We examine the conditions required to trigger HSC, study the role of expansion velocity, and discuss our results in relation to GRB prompt emission. We find multi-pulse light curves from slowly expanding regions ($u_{\text{exp}} \lesssim 0.01c$) that are a manifestation of the natural HSC quasi-periodicity, while single-pulse light curves with a fast rise and slow decay are found for higher velocities. The formation of the photon spectrum is governed by an in-source electromagnetic cascade. The peak photon energy is ~ 1 MeV (~ 1 GeV) for maximum proton energies $\sim 1 - 10$ PeV ($1 - 10$ EeV) assuming a jet Lorentz factor 100. Peak γ -ray luminosities are in the range $10^{49} - 10^{52}$ erg s⁻¹, with the MeV-peaked spectra being $\sim 100 - 300$ times more luminous than their GeV-peaked analogues. HSC bursts peaking in the MeV are also copious ~ 10 TeV neutrino emitters, with an all-flavour fluence $\sim 10\%$ of the γ -ray one. The hypothesis that typical long-duration GRBs are powered by HSC could be tested in the near future with more sensitive neutrino telescopes like IceCube-Gen2.

Key words: instabilities - radiation mechanisms: non-thermal -adiabatic expansion-gamma-ray burst prompt emission: general

1 INTRODUCTION

Gamma Ray Bursts (GRBs) are brief flashes of γ -rays and are considered to be one of the most energetic transient explosive phenomena in the universe. The production mechanism of a GRB remains still a challenging problem in high-energy astrophysics since their first discovery more than a half century ago. The main phase of the GRB phenomenon, namely the prompt emission phase, is associated with several notable characteristics, such as the high photon luminosity and highly variable light curves¹, usually consisting of many pulses, each of them lasting from 1 msec to 1 sec. The GRB prompt emission can last in total from seconds to minutes, i.e., less than 2 s in the case of short GRBs and more than 100 s in the case of long GRBs, reaching luminosities up to $L_{\gamma} = 10^{54}$ erg s⁻¹ (for reviews see Kumar & Zhang (2015); Beloborodov & Mészáros (2017)). In the last several years, a number of GRB events with considerable longer duration has been detected. These outbursts, named Ultra Long GRBs (UL-GRBs), are characterised by a γ -ray emission that lasts for several thousands of seconds (Gendre et al. 2013). In general, the spectrum of prompt emission has a well defined peak at an energy ε_{pk} that typically lies in the range of 0.1 – 1 MeV. Some years ago the Fermi Large Area Telescope (LAT) detected GeV photons from several

GRBs and in some cases it found additional spectral components in the GeV energy range (Abdo et al. 2009; Ackermann et al. 2011; Goldstein et al. 2012). A general feature is that the onset of the GeV emission tends to be delayed up to some seconds, relatively to the onset of the main MeV emission, suggesting a likely different origin of these photons. More recently, ground-based Cherenkov telescopes have detected even higher energy photons, i.e., greater than 100 GeV, in the early afterglow of certain GRBs (MAGIC Collaboration et al. 2019; Abdalla et al. 2019), suggesting that GRBs can be one of the most extreme astrophysical accelerators in the universe.

The majority of the GRB spectra in the prompt emission phase are well fitted by the so-called Band function (Band et al. 1993), which consists of two power laws smoothly connected at the energy ε_{pk} . Although various models have been proposed during the past few decades, the radiation mechanisms responsible for the prompt GRB emission remain still a puzzle. Generally, there are two classes of models for GRB emission depending on the species of the radiating particles, namely the leptonic and the hadronic ones. In the leptonic scenario, electron synchrotron radiation was one of the first mechanisms proposed to explain the prompt GRB emission (Katz 1994; Meszaros et al. 1994; Sari et al. 1996; Sari et al. 1998). However, the optically thin electron synchrotron model faced several theoretical difficulties, such as the *line of death* problem, that refers to the discrepancy between the observed and model predicted low energy photon index. (Crider et al. 1997; Preece et al. 1998). A refined time-dependent spectral analysis in several bright bursts (Guiriec 2012; Oganessian et al. 2017, 2019) has shown that the GRB spectra may

* E-mail: iflorou@phys.uoa.gr

† E-mail: amastich.phys.uoa.gr

‡ Mercator Fellow

¹ In some cases the GRB light curves consist of a single pulse that shows a Fast Rise and an Exponential Decay (FRED).

be better fitted with a multi-component model or with a phenomenological function consisting of two broken power laws instead of the classical Band function. The availability of more detailed spectral information has led the GRB community to readdress the electron synchrotron model as the main radiative mechanism responsible for the prompt emission for the majority of GRBs. [Burgess et al. \(2020\)](#) have performed a time resolved spectral analysis to the prompt spectra of single pulse GRBs, detected by the FERMI Gamma Ray Monitor (GBM), and have concluded that the electron synchrotron interpretation is a feasible option once time dependence and cooling are properly included.

Proton synchrotron radiation was also proposed to explain the prompt GRB emission ([Ghisellini et al. 2020](#)), motivated by recent spectral analysis of GRBs detected by the Swift Burst Alert Telescope (BAT) ([Oganesyan et al. 2017, 2019](#)). However, it was recently demonstrated that the proposed scenario cannot explain the observed GRB spectra, unless very high bulk Lorentz factors (> 1000) are assumed, implying a very high required jet power, i.e. $\gtrsim 10^{54}$ erg s^{-1} ([Florou et al. 2021](#)). Still, proton synchrotron radiation is typically used to explain the high-energy part of the γ -ray spectrum (greater than 100 MeV) ([Vietri 1997; Totani 1998; Asano et al. 2009; Razaque 2010](#)), while the sub MeV photons are produced by primary electrons that also emit synchrotron radiation ([Dermer & Atoyan 2003](#)). This scenario has been applied to explain the underlying power-law components seen in some bright Fermi-LAT bursts in the GeV energy band ([Racusin et al. 2008; Abdo et al. 2009](#)). Another scenario for the production of the high-energy part of the spectrum are proton induced cascades ([Dermer & Atoyan 2006; Asano & Inoue 2007](#)). In any case, hadronic models pose an attractive alternative to the leptonic ones for the GRB emission mechanism; they make predictions for ultra-high energy cosmic ray production ([Vietri 1995; Waxman 1995; Murase et al. 2008](#)) and high-energy neutrino emission ([Waxman & Bahcall 1997; Murase 2008; Gao et al. 2012](#)) that are testable with existing (e.g., IceCube Neutrino Telescope and future experiments, e.g. IceCube Gen2, the KM3NeT Open Science System ([Aartsen et al. 2021a; Schnabel et al. 2021](#))).

A disadvantage of hadronic models, when applied to GRBs, is their low radiative efficiency, i.e. one needs very large luminosities in protons in order to produce the required GRB γ -ray luminosity. However, under certain circumstances, a hadronic system undergoes an abrupt transition from a radiatively inefficient to a radiatively efficient state, often exhibiting flaring activity. This intriguing property of hadronic systems is coined as hadronic supercriticality (HSC) and many of its properties can be related to the GRB prompt emission ([Kazanas et al. 2002; Mastichiadis & Kazanas 2009; Petropoulou et al. 2014; Petropoulou & Mastichiadis 2018; Mastichiadis et al. 2020](#)). The relativistic protons inside the source become supercritical once a feedback and a marginal stability criterion are simultaneously satisfied, as first demonstrated by the stability analysis of [Kirk & Mastichiadis \(1992\)](#). As far as the feedback criterion is concerned, [Kirk & Mastichiadis \(1992\)](#) and [Petropoulou & Mastichiadis \(2012\)](#) showed that the network of processes that play a key role in the manifestation of supercriticality are synchrotron radiation, photohadronic interactions and $\gamma\gamma$ pair production. Three feedback loops are created between these physical processes that are responsible for the state transition described above. The marginally stability criterion has to do with the value of the relativistic proton column density inside the source. In case it exceeds a critical value the system behaves non linearly and bears similarities to the Lotka-Volterra type of systems that describe a prey-predator relation between protons and photons. In this project we expand the work of [Petropoulou et al. \(2014\); Petropoulou & Mastichiadis \(2018\); Mastichiadis et al. \(2020\)](#), which assumed an

emitting region of constant volume and magnetic field, by investigating for the first time the same phenomenon in adiabatically expanding sources.

This paper is structured as follows: In Sec. 2 we investigate analytically how the supercritical behaviour can be affected by the expansion of the source. We next present in Sec. 3 our methodology and the numerical code that we utilise. In Sec. 4 we investigate numerically the effect of the expansion on the manifestation of supercriticality. In Sec. 5 we discuss our results in the context of GRB prompt emission. For this, we compute the spectrum and light curve of a fiducial GRB powered by several expanding blobs ejected by the central engine. Finally, we summarise and discuss our results in Sec. 6. For the GRB application we adopt $z = 2$ as a typical redshift and use $H_0 = 69.32$ km Mpc $^{-1}$ s $^{-1}$, $\Omega_M = 0.29$, $\Omega_\Lambda = 0.71$ ([Hinshaw et al. 2013](#)). Quantities denoted with the superscript/subscript ‘obs’ refer to the observer’s frame, while the rest to the comoving frame of the outflow.

2 FIRST PRINCIPLES

In the non expanding case, the HSC manifests itself when the proton energy density inside the source exceeds some critical value – see [Mastichiadis et al. \(2020\)](#) for a comprehensive study. The above requirement poses a marginal stability criterion, according to which, above the critical proton density, the system becomes highly efficient, transferring the stored proton energy into secondary particles, namely photons, electron/positron pairs and neutrinos. Previous work on the manifestation of supercriticality in non expanding systems, has shown that this hadronic non linear behaviour arises as a result of specific networks of physical processes (feedback loops). For example, [Kirk & Mastichiadis \(1992\)](#) showed that synchrotron photons of the relativistic electron-positron pairs, produced via photo-pion/photo-pair interactions, become targets for the relativistic protons, which then produce even more pairs and pions. This feedback loop leads to an exponential photon outgrowth and eventually to fast proton energy losses. Another type of feedback network was examined by [Petropoulou & Mastichiadis \(2012\)](#), according to which γ -rays, that are produced directly via proton synchrotron or indirectly via photo-pair and photo-pion interactions, turn spontaneously into electron-positron pairs and eventually in soft photons, which become targets for the relativistic protons and feedback on them.

The system enters the supercritical regime in various ways, the most interesting being with multiple photon bursts that occur quasi periodically (limit cycles) when the number density of protons slightly exceeds the critical value. For even higher proton densities, the number of bursts in the light curve is increased. However, if the proton number density keeps increasing the temporal behaviour of the system degenerates to a single burst before it saturates into a highly efficient steady state. As it was shown in [Mastichiadis et al. \(2020\)](#), the critical proton density depends on several source parameters like the radius of the source, the magnetic field strength and the specifics of the proton distribution (minimum/maximum proton Lorentz factors and the power law slope assuming that it is a power law). The main question that we are going to address in the present project is whether the supercritical behaviour persists when the source is spherically expanding and (if yes) how it manifests itself.

We begin our analysis by assuming an expanding spherical volume of instantaneous radius:

$$r = r_{\text{in}} + u_{\text{exp}}(t - t_{\text{in}}). \quad (1)$$

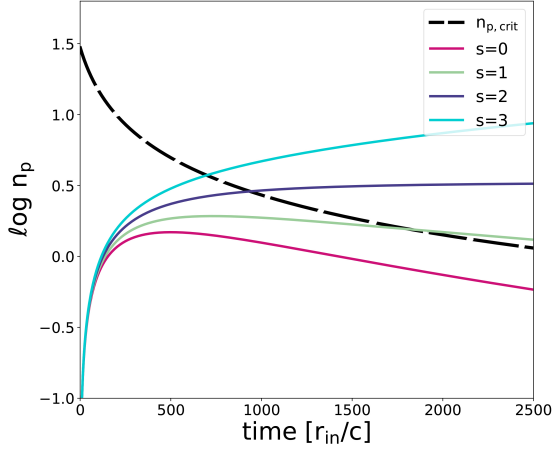


Figure 1. The proton number density derived from eq. 4, in arbitrary units, as a function of time, expressed in r_{in}/c units, for a fixed value of the expansion velocity, $u_{\text{exp}} = 10^{-3}c$, and different values of the proton luminosity injection index s . The dashed black line corresponds to the marginal stability criterion for the PeS loop (see eq. 6).

Here u_{exp} is the expansion velocity which we assume to be constant, t is the time, t_{in} is the initial moment of the particle injection inside the source volume and r_{in} the initial radius of the source.

In the case of no particle escape and negligible energy losses, the differential equation which describes the evolution of the number density of an energy integrated proton distribution inside the source, is given by:

$$u_{\text{exp}} \frac{dn_p}{dr} + \frac{3u_{\text{exp}}n_p}{r} = Q_p, \quad (2)$$

where Q_p is the proton injection rate per unit volume:

$$Q_p(r) = Q_{p,0} \left(\frac{r}{r_{\text{in}}} \right)^{s-3}, \quad (3)$$

$Q_{p,0}$ is a normalisation factor and s is an index that determines the rate of energy injection as the source expands. We take as an initial condition that $n_p(r_{\text{in}}) = 0$. The solution of eq. 2, for $s \neq -1$, is given by the following relation:

$$n_p(r) = \frac{Q_{p,0}r^{s-2}}{u_{\text{exp}}(s+1)} - \frac{Q_{p,0}r_{\text{in}}^{s+1}}{u_{\text{exp}}(s+1)r^3}, \quad (4)$$

while in the case $s = -1$, the solution is:

$$n_p(r) = \frac{Q_{p,0} \ln(r/r_{\text{in}})}{u_{\text{exp}}r^3}. \quad (5)$$

As it can be seen from the above relations, since the initial condition is $n_p(t_{\text{in}}) = 0$, at early times proton injection will cause an increase in the number density, which will reach a maximum, for the cases where $s < 2$, and then will drop for $r \gg r_{\text{in}}$. For $s > 2$ the proton number density will keep increasing, while in the case of $s = 2$, it will reach asymptotically a constant value.

Figure 1 illustrates the evolution of the proton number density (see eq. 4) with time (in r_{in}/c units), for different values of the proton luminosity injection index s (coloured lines). As an example, we also plot, with a black dashed line, the critical proton density required to reach the marginal stability criterion for the PeS feedback loop (Kirk & Mastichiadis 1992). This is formed when the synchrotron photons

radiated from the photo-pair secondaries produce even more pairs on the protons before they escape from the source. The critical number density $n_{p,\text{crit}}$, for a proton Lorentz factor γ , is expressed according to the following relation:

$$n_{p,\text{crit}} = \left(\frac{2}{3}p - 1 \right) b^{1-p/3} \left(\int_2^{b\gamma^3} \sigma_{\text{pe}}(y)y^{-1-p/3} dy \right)^{-1} r^{-1}. \quad (6)$$

This expression has been derived for a proton power-law distribution with index p . In the example shown in Fig. 1 we used $p = 2$. The lower limit of the integral is the threshold of the photo-pair interaction (in units of $m_e c^2$), while the upper limit is the relation that defines the critical value of proton Lorentz factor for which the PeS feedback loop operates, i.e. $b\gamma^3 \geq 2$. Here $b = B/B_{\text{crit}}$, B the magnetic field inside the source, while $B_{\text{crit}} = 4.4 \times 10^{13}$ G is the Schwinger magnetic field and σ_{pe} is the cross section of the photo-pair interaction. For the specific example shown in Fig. 1 we have used $B = 10^4$ G.

For all practical purposes, we assume that when the curve critical proton density intersects the curves of the proton densities, then the system enters the supercritical regime. The critical proton density decreases as $1/r$ (see eq. 6) as the source expands (assuming a constant magnetic field). Therefore it will always intersect the curves with $s \geq 2$, while it might or it might not intersect the ones for $s < 2$, depending on $Q_{p,0}$. This is illustrated in Fig. 1 where $n_{p,\text{crit}}$ (black dashed line) intersects the proton number density for $s = 1$ (green line) but not for $s = 0$ (pink line). In this latter case one would have to increase the value of $Q_{p,0}$ in order to bring the system in the non linear regime. Therefore, the onset of supercriticality becomes more luminosity demanding, as the value of proton luminosity injection index becomes smaller. Furthermore, inspection of eqs. 4 and 5 reveals that when the velocity of expansion becomes higher and $s < 2$, the system can become supercritical only for higher values of the proton injection rate.

If one integrates over time the coloured curves depicted in Fig. 1 until the moment each one intersects the black dashed line, the results are similar in all cases. In other words, even though the proton injection rates needed for the onset of a supercritical flare are higher for $s < 2$ compared to those for $s \geq 2$, the proton column density needed for supercriticality is independent of s . This is reminiscent of nuclear piles (Kazanas et al. 2002; Mastichiadis & Kazanas 2009).

3 THE NUMERICAL CODE

In order to study the full problem, taking into account all the radiative processes, we have to solve the proton, photon and electron/positron kinetic equations numerically. We consider, as previously, a spherical source of initial radius r_{in} that expands adiabatically with a constant velocity u_{exp} . The emitting region contains a tangled magnetic field of strength B , which varies with r as the source expands according to:

$$B = B_{\text{in}} \left(\frac{r_{\text{in}}}{r} \right)^q \quad (7)$$

where B_{in} is the value of the magnetic field at $r = r_{\text{in}}$.

We assume that pre-accelerated relativistic protons are injected in the source, having a power-law energy distribution with a luminosity depending on the location of the emitting region in the jet, expressed as:

$$L_p(r) = L_{p,\text{in}} \left(\frac{r}{r_{\text{in}}} \right)^s \quad (8)$$

where $L_{p,\text{in}}$ is the proton injection luminosity at the initial radius of

the source. The proton injection luminosity is related to the differential proton injection rate, which enters the equations we have to solve, as:

$$Q_p(\gamma, r) = \frac{L_p(r)}{(m_p c^2)^2 \int_{\gamma_{\min}}^{\gamma_{\max}} \gamma^{-p+1} d\gamma}, \quad (9)$$

where $Q_p(\gamma, r)$ is defined as:

$$Q_p(\gamma, r) \equiv \frac{dN_p}{d\gamma dr} = Q_i(r) \gamma^{-p} H(\gamma - \gamma_{\min}) H(\gamma_{\max} - \gamma) H(r - r_{\text{in}}) \quad (10)$$

and the proton injection per volume:

$$Q_p(\gamma, r) = \frac{3Q_p(\gamma, r)}{4\pi r^3} \quad (11)$$

For the definition of $Q_p(\gamma, r)$ see the previous section. In eq. 10 $H(x)$ is the Heaviside step function, $\gamma_{\min}, \gamma_{\max}$ are the minimum and maximum proton Lorentz factors, respectively, and Q_i is a radially dependent normalisation factor. Since we assume that γ_{\min} and γ_{\max} remain constant throughout the evolution of the system, the above relations imply that $Q_i \propto r^{-s}$.

It is also useful to define a measure of the proton luminosity in terms of the proton compactness:

$$\ell_p = \frac{\sigma_T L_p}{4\pi r m_p c^3} = \ell_{p,\text{in}} \left(\frac{r}{r_{\text{in}}} \right)^{s-1} \quad (12)$$

Similarly, we define the instantaneous photon compactness ℓ_γ :

$$\ell_\gamma = \frac{\sigma_T L_\gamma}{4\pi r m_e c^3} \quad (13)$$

where L_γ is the bolometric photon luminosity of the source.

Protons, electrons and photons are the three stable species inside the source. We assume that pions and muons decay instantaneously, neutrons do not interact with soft photons, and neutrinos escape the source freely. The evolution of the stable particle populations inside the spherical volume can be described by a system of coupled integro-differential kinetic equations:

$$\frac{\partial n_j}{\partial t} + u_{\text{exp}} \frac{3n_j}{r(t)} + \frac{n_j}{t_{\text{esc},j}} + \mathcal{L}_j = Q_j \quad (14)$$

where the index j refers to protons (denoted as p), electrons/positrons (denoted as e) and photons (denoted as γ), $t_{\text{esc},j}$ is the escape timescale from the source, and n_j is the differential number density of each species. We assume that all charged particles remain confined in the blob ($t_{\text{esc},p/e} \rightarrow \infty$) and only photons escape on a timescale $t_{\text{esc},\gamma} = r/c$ (same for neutrons and neutrinos). The loss (\mathcal{L}_j) and injection (Q_j) per volume terms² include the following processes (for details see [Mastichiadis & Kirk 1995](#)):

- synchrotron radiation for both electrons and protons
- proton-photon pair production (photopair)
- proton-photon pion production (photopion)
- synchrotron self-absorption
- electron inverse Compton scattering
- photon-photon ($\gamma\gamma$) pair production
- electron-positron pair annihilation
- adiabatic losses, as described in [Kardashev \(1962\)](#).

² For protons the injection operator is given by eq. 11, and is equal to zero for relativistic primary electrons.

We develop a new numerical code starting from the one of [Mastichiadis & Kirk \(1995, 1997\)](#) that was applicable to non expanding sources. This new version solves the system of coupled integrodifferential described by eq. 14, and gives the evolution of the distribution of the stable particle populations as a function of the continuously changing comoving source radius. We note that we treat the synchrotron and inverse Compton scattering as full emissivities while we take delta-function approximations for the photopion process. A first version of this code which contains only leptonic processes has been presented recently in [Boula & Mastichiadis \(2022\)](#) in application to the non-thermal emission from AGN.

The free parameters of the problem are the initial radius r_{in} and magnetic field strength B_{in} of the source, the power-law index of the magnetic field radial profile q , the initial proton compactness $\ell_{p,\text{in}}$, the power-law index of the proton injection radial profile s , the maximum proton Lorentz factor γ_{\max} and the expansion velocity u_{exp} . We assume that $\gamma_{\min} = 1$ and $p = 2$, and we take as an initial condition that $n_j(\gamma_j, r_{\text{in}}) = 0$.

4 HSC IN EXPANDING SOURCES

In this section we examine numerically the effects of the expansion on the onset and phenomenology of HCS.

4.1 Comparison to non expanding sources

We begin the numerical investigation by examining the modification that expansion would bring to the onset of HSC. To have the closest possible analogy with the non expanding case, we neglect adiabatic losses while we assume that the magnetic field and proton injection luminosity do not change with radius, i.e. $q = 0$ and $s = 0$ respectively. We then select a low value for the expansion velocity, $u_{\text{exp}} = 10^{-2.5}c$ and use a set of parameter values that would drive a non expanding source to supercriticality, namely $\ell_{p,\text{in}} = 10^{-3}$, $r_{\text{in}} = 10^{11}$ cm, $\gamma_{\max} = 10^4$, and $B_{\text{in}} = 10^4$ G. Nevertheless, when the system expands the numerical result is a subcritical light curve, as depicted in grey on the top panel of Fig. 2. We start increasing $\ell_{p,\text{in}}$ until we find a value that produces one supercritical flare (teal solid curve on the top panel of Fig. 2). This value, at least within the accuracy of our numerical resolution, marks the onset of the HSC in this case and we denote it as $\ell_{p,\text{crit}}$. From there on, we progressively increase $\ell_{p,\text{in}}$, by a factor of 0.2 in logarithmic scale and record the system's response. As in the non expanding case, multiple outbursts occur more frequently as the compactness increases, while the first flare in each case progressively appears at earlier times. For even higher proton compactnesses, the system enters supercriticality but saturates very quickly with the photon compactness reaching a constant value (light blue solid curve on the top panel of Fig. 2).

Overall, our results are analogous to those of previous works on HSC for non expanding systems. Nonetheless, there are two main differences. First, the non linear behaviour in an expanding source is achieved at the cost of higher proton luminosities; a higher injection rate of protons is needed to counterbalance the effects of expansion and to reach the critical number density (see Sec. 2). Second, the duration of flares in the supercritical regime increases with time as a result of the source expansion (see, e.g. the red and yellow coloured light curves in Fig. 2).

We can summarise the phenomenology of the system with increasing proton luminosity as follows: subcritical steady state \rightarrow one supercritical flare \rightarrow multiple supercritical flares \rightarrow a single flare that quickly merges into a supercritical steady state.

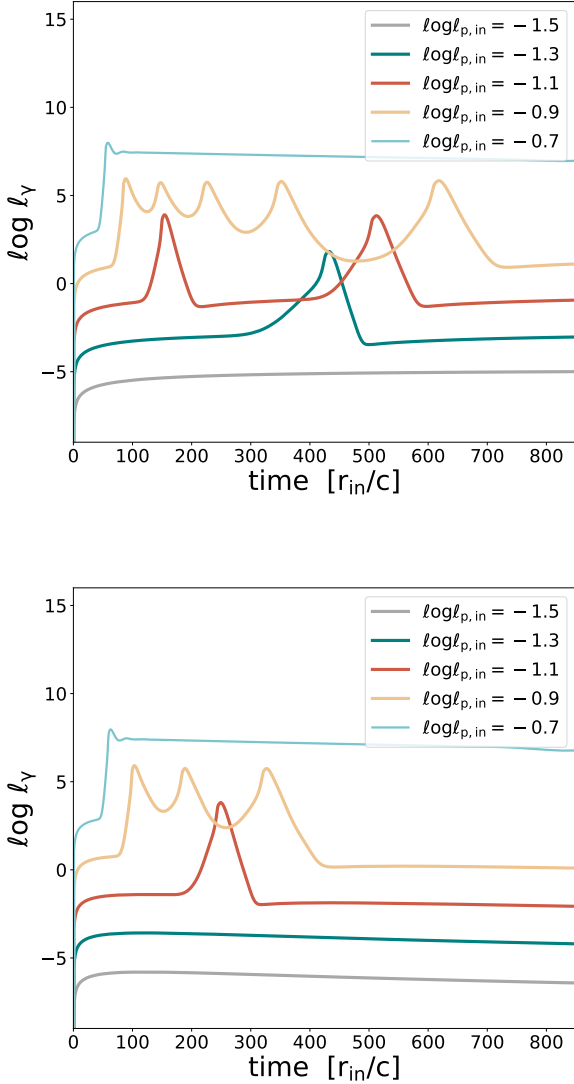


Figure 2. Top panel: logarithmic plot of photon compactness as a function of time in r_{in}/c units, for various values of the initial proton injection compactness that differ by a factor of 0.2 in logarithm. The source magnetic field is constant ($q = 0$). For better readability, each curve is shifted from the previous one by a factor of 2. Bottom panel: Same as in the top panel but for a decaying magnetic field ($q = 1$). In both panels the source is expanding with velocity $u_{\text{exp}} = 10^{-2.5}c$. Other parameters used are: $B_{\text{in}} = 10^4$ G, $r_{\text{in}} = 10^{11}$ cm, $\gamma_{\text{max}} = 10^4$ and $s = 0$.

4.2 The effect of the magnetic field radial profile

We now extend our analysis by examining the more realistic case where the magnetic field is decreasing as the source volume increases – see Fig 2, bottom panel. Choosing exactly the same initial conditions that produced the light curves on the top panel of Fig. 2 but letting B to vary as r^{-1} we find that one needs to increase the proton luminosity for the system to enter the supercritical regime – compare teal and red lines in the top and bottom panel of Fig. 2. Even when well inside the supercritical regime, the number of bursts tends to decrease when B decreases with distance – compare the orange lines in the top and bottom panels of Fig. 2, making, thus,

the HSC less efficient. As expected, this trend is intensified when B drops faster with distance. We therefore conclude that the decrease of the magnetic field as the source expands tends to suppress the HSC. Note, however, that its basic characteristic features are still there.

4.3 The effect of expansion velocity

We investigate next how the supercritical behaviour is affected by the expansion velocity. We choose the same set of parameters as the ones used for the top panel of Fig. 2. Initially we choose a very low value for expansion velocity in order to have an estimate of the system’s behaviour in the limiting case of no expansion. For $u_{\text{exp}} = 10^{-4}c$ the first supercritical flare appears at $4000 r_{\text{in}}/c$ (black solid line in Fig. 3). This is the minimum time that is needed for producing at least one photon outburst (henceforth, T_{B}), and is a function of model parameters, i.e. $T_{\text{B}} = f(B_{\text{in}}, \gamma_{\text{max}}, u_{\text{exp}}, s, q)$. If we start increasing the expansion velocity, e.g. $u_{\text{exp}} = 10^{-3.5}c$, while keeping all other parameters the same, the supercritical behaviour is lost. This is due to the fact that the increase of the expansion velocity leads to a decrease of the proton density and as a result the marginal stability criterion is never met. In order to recapture this condition one needs to increase the injected proton luminosity. In this case the system shows a flare earlier than before (see blue light curve in Fig. 3). This procedure is repeated for greater values of the expansion velocity (see coloured light curves of Fig. 3) and a similar behaviour is found, i.e. the larger the value of expansion velocity, the earlier the appearance of the first supercritical flare. This occurs, however, at the expense of more proton luminosity. These results are in total agreement with our analysis in Sec. 2.

We then explore the temporal behaviour of the system for different values of the expansion velocity following the procedure outlined in Sec. 4.1. For each light curve depicted in Fig. 3 we increase the value of $\ell_{\text{p},\text{in}}$ and record the shape of the produced light curve. We find that as the expansion velocity increases, the number of multiple bursts decreases and finally, for $u_{\text{exp}} > 10^{-2}c$, it reduces to a single burst (not explicitly shown here). This phenomenology is similar to the one shown in Fig. 2. We also note that the increase of the expansion velocity leads to the production of broader photon pulses. The width of the pulse is related to the light crossing time of the emitting source, which is larger for higher values of u_{exp} at a given time. Moreover, the system’s radiative efficiency, defined as the ratio of the total radiated energy in photons to the total injected energy in relativistic protons within a constant time interval, decreases as the source expands faster.

4.4 The effects of adiabatic losses and of the proton luminosity profile

All results presented so far were derived without taking into account the adiabatic losses in the kinetic equations of protons and electrons. These are not expected to be important for most parameters studied here, except for the lowest energy particles. We therefore repeated the calculations shown in Fig. 3 after including adiabatic energy losses and record the $\ell_{\text{p},\text{crit}}$ that is needed to bring the system to supercriticality. The results are plotted as a function of u_{exp} in Fig. 4 (dashed black line) and should be compared with those obtained without adiabatic losses (solid black line). The difference in the required proton injection compactness between the two cases is negligible, except for high expansion velocities where differences up to a factor of ~ 3 are found.

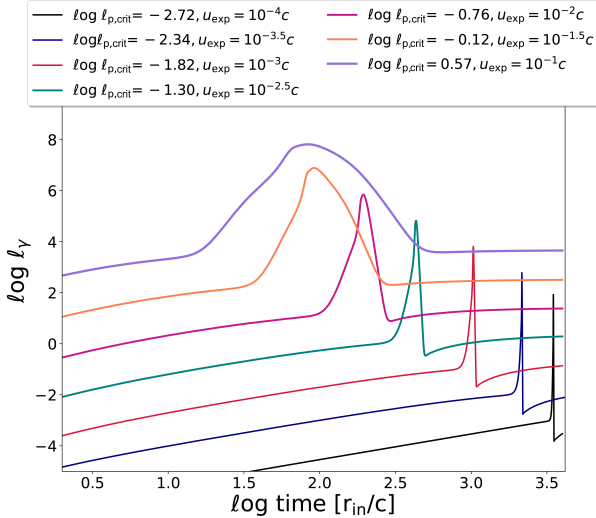


Figure 3. A log-log plot of photon compactness as a function of time in r_{in}/c units, for different values of u_{exp} and $\ell_{\text{p,crit}}$. Each light curve is shifted from the previous one in the y-axis one order of magnitude to make the plot easier to read. Other parameters are: $r_{\text{in}} = 10^{11}$ cm, $B_{\text{in}} = 10^4$ G, $\gamma_{\text{max}} = 10^4$, $q = 0$, $s = 0$.

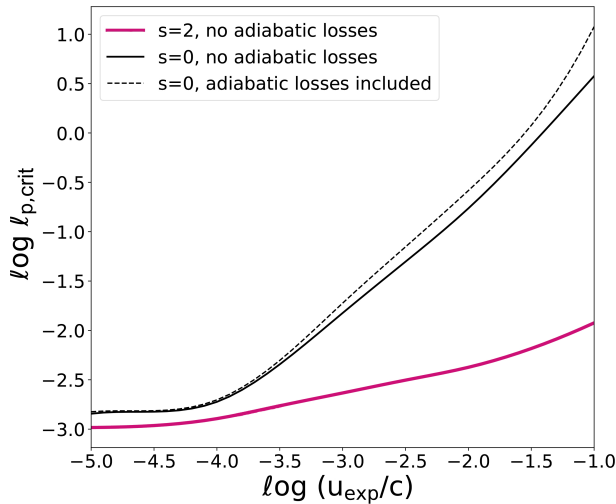


Figure 4. Plot of $\ell_{\text{p,crit}}$ as a function of u_{exp} for $s = 0$ without adiabatic losses for particles included (black solid line), $s = 0$ with adiabatic losses of particles included (dashed black line), and $s = 2$ (magenta solid line). All other parameters are the same as in Fig. 3.

Another parameter that plays a role in the appearance of supercriticality is the radial profile of the proton luminosity. In all the above we have assumed that the proton luminosity is independent of the source radius (and location along the jet). We therefore repeated the calculations used for the construction of Fig. 3 with the same parameters, except for the injected proton luminosity index s . As we have already demonstrated with a simple model in Sec. 2, the increase of s makes the appearance of supercriticality less luminosity demanding. This is demonstrated in Fig. 4 where $\ell_{\text{p,crit}}$ is plotted

for $s = 2$ as a function of expansion velocity (solid magenta line). The difference with the case where $s = 0$ is that for $s \geq 2$ one can always find one supercritical flare for a fixed proton compactness value, even when the source expands with a fast velocity. In the case of very slow expansion, e.g. $u_{\text{exp}} = 10^{-4}c$, a supercritical flare is produced at $T_{\text{B}} = 4000 r_{\text{in}}/c$. As we have already mentioned, this value depends on the set of chosen source parameters. For higher expansion velocity values and the same $\ell_{\text{p,crit}}$ this supercritical flare is found at later moments. We therefore increase the $\ell_{\text{p,in}}$ in order to fix the appearance of the flare at $T_{\text{B}} = 4000 r_{\text{in}}/c$. We conclude that the proton compactness is lower than the corresponding value for $s = 0$. However, the amount of proton energy required for the system to become supercritical is independent of s , in agreement with our analytical findings (see Sec. 2).

5 RELEVANCE TO GRB PROMPT EMISSION

5.1 Energetics and photon spectra

In this section we discuss HSC in the context of GRB prompt emission. We assume that at a distance R_{γ} from the central engine protons are accelerated to a power law and are subsequently injected into a spherical region with radius $r = R_{\gamma}/\Gamma$ as measured in the jet comoving frame. The assumption of the spherical geometry is valid as long as the beaming angle $1/\Gamma$ is smaller than the opening angle of the GRB jet. This spherical region moves away from the central engine with a bulk Lorentz factor Γ and is expanding with a velocity u_{exp} .

We fix $r_{\text{in}} = 10^{11}$ cm, $B_{\text{in}} = 10^4$ G, which can be considered as nominal values for GRBs, and run the code for different values of the maximum proton Lorentz factors in the range $10^4 - 10^8$. We numerically verified that for $\gamma_{\text{max}} \leq 10^4$ the multi-burst behaviour is lost. We therefore exclude these Lorentz factors from the analysis. As an indicative example, we take the magnetic field of the emitting region to drop linearly with radius (i.e. $q = 1$) as the source is expanding, and the proton injection luminosity to increase as $s = 1$. Finally, we assume that the shell expands adiabatically having an expansion velocity equal to $u_{\text{exp}} = 10^{-2.5}c$. For the transformation of quantities from the comoving to the observer's frame we use $\Gamma = 100$.

We inject relativistic protons in the source until T_{B} , which as we discussed in Sec. 4.3, is the minimum time that is needed for producing at least one photon outburst, depending of the chosen set of parameters. For the adopted parameter values, we find that $T_{\text{B}} \approx 400 r_{\text{in}}/c$ in the case where $u_{\text{exp}} = 10^{-2.5}c$ and $s = 1$. After searching for the minimum initial proton compactness (for a given γ_{max}) required for the onset of supercriticality, we perform consecutive runs by increasing this value by a factor of 0.1 in logarithmic scale. For each case we compute the total energy in relativistic protons (in the observer's frame) injected in the time interval between $t_{\text{in}} = 0$ and T_{B} :

$$E_{\text{p,tot}}^{\text{obs}} = \Gamma^3 (1+z) \int_{t_{\text{in}}}^{T_{\text{B}}} L_{\text{p}}(t) dt. \quad (15)$$

where $L_{\text{p}}(t)$ is calculated from eq. 12 and time t is related to the radius through eq. (1). We also calculate the bolometric photon energy (in the observer's frame) released during the same time interval:

$$E_{\gamma,\text{tot}}^{\text{obs}} = \Gamma^3 (1+z) \int_{t_{\text{in}}}^{T_{\text{B}}} L_{\gamma}(t) dt. \quad (16)$$

where $L_{\gamma}(t)$ is calculated by eq. 13. We then construct a two-dimensional plot of the total proton energy used as a function of

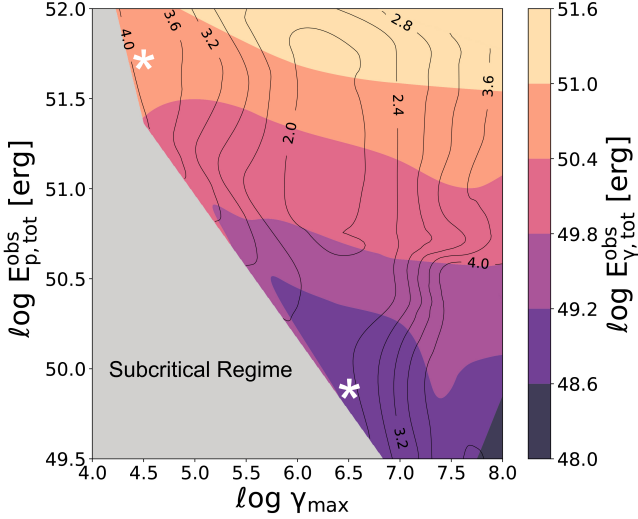


Figure 5. Phase space of the total proton energy injected in the expanding source for a time period of $T_B = 400 r_{\text{in}}/c$ as a function of the maximum proton Lorentz factor. The coloured region corresponds to the supercritical regime while the grey space to the linear subcritical regime. Colours represent the bolometric photon energy released, while contours show the ratio of the proton density to magnetic field density $U_{p,\text{pk}}/U_{B,\text{pk}}$ at the peak of the first flare. The model parameters are $r_{\text{in}} = 10^{11}$ cm, $B_{\text{in}} = 10^4$ G, $q = 1$, $s = 1$, $u_{\text{exp}} = 10^{-2.5}c$, $\Gamma = 100$ and $z = 2$. White asterisks indicate two cases whose spectra and light curves are displayed in Fig. 5.

the maximum proton Lorentz factor and show the result in Fig. 5. The coloured region corresponds to the supercritical regime, with colour indicating $E_{\gamma,\text{tot}}^{\text{obs}}$, while the grey shaded region indicates the subcritical regime. For the smaller and larger values of the maximum proton Lorentz factor that we explored, i.e. $\gamma_{\text{max}} = 10^4 - 10^5$ and $\gamma_{\text{max}} = 10^{6.5} - 10^8$ respectively, the light curves exhibit multiple bursts for most values of the proton initial compactness. Only when $\ell_{p,\text{in}}$ surpasses a certain value the multiple bursts blend into a single burst, as it was shown in Fig. 2. For intermediate values of the maximum proton Lorentz factor, however, i.e. $\gamma_{\text{max}} = 10^{5.5} - 10^6$ we find only single-pulse supercritical light curves. This behaviour is similar to the one found for the non-expanding source by Mastichiadis et al. (2020).

For a fixed value of $E_{p,\text{tot}}^{\text{obs}}$ the photon energy output is almost independent of γ_{max} , as indicated by the almost horizontal stripes of the same colour in Fig. 5. As the maximum proton Lorentz factor decreases, e.g. $\gamma_{\text{max}} = 10^4 - 10^5$, more energy has to be injected into protons to produce supercritical photon outbursts. HSC is an efficient process for converting proton energy into photon energy, as suggested by the values of $E_{\gamma,\text{tot}}^{\text{obs}}/E_{p,\text{tot}}^{\text{obs}}$ that range between 0.03 and 0.4. Moreover, the values of the bolometric photon energy that we find fall within the range of values deduced from GRB prompt emission observations. Finally, the contours shown in the same figure indicate the ratio of the proton energy density to magnetic energy density $U_{p,\text{pk}}/U_{B,\text{pk}}$, at the moment of the peak of the first supercritical flare. It appears that in the supercritical regime the condition $U_{p,\text{pk}} \gg U_{B,\text{pk}}$ must be satisfied.

We next choose two indicative parameter sets from Fig. 5 to look more closely into their spectra and light curves. Both cases belong to the supercritical regime and have very different γ_{max} and $E_{p,\text{tot}}^{\text{obs}}$ values (see white asterisks). We show the results for $\gamma_{\text{max}} = 10^{4.5}$ and $10^{6.5}$ on the left and right panels of Fig. 6, respectively. The central plot

in both panels presents snapshots of the observed broadband photon spectra during the rising part of the first pulse of the light curve as indicated in the inset plots. Each spectrum differs from the previous one by r_{in}/c . We use a colour scale to better illustrate the temporal evolution of the spectra in the observer’s frame (see colourbar on the right of each plot). As it can be seen in Fig. 6, the photon spectra show distinctive peaks coming from the reprocessing of radiation due to non linear cascades initiated by the feedback loops (see black solid line on the left panel). Therefore these spectral features are only indirectly related to the choice of γ_{max} . For the particular example shown in the left panel, the proton luminosity required for the system to enter the supercritical regime is rather high (see Fig. 5), therefore the reprocessing is strong causing the photon spectrum to peak at an energy $\varepsilon_{\text{pk}}^{\text{obs}}$ around \sim MeV in the observer’s frame. For higher values of γ_{max} , however, the proton luminosity requirements for entering the supercritical regime are relaxed and the photon spectral peak moves to higher energies.

This trend becomes also evident in Fig. 7, which depicts a plot of the photon luminosity at the maximum of the light curve $L_{\gamma,\text{pk}}^{\text{obs}}$ versus $\varepsilon_{\text{pk}}^{\text{obs}}$, in the observer’s frame, for various values of γ_{max} shown in the colour bar. Clearly the obtained photon luminosities fall in the range of the ones observed from GRBs. However, only the lower values of γ_{max} yield photon spectra with $\varepsilon_{\text{pk}}^{\text{obs}} \sim 1$ MeV. For $\gamma_{\text{max}} \gtrsim 10^{6.5}$, the photon spectra peak at $\varepsilon_{\text{pk}}^{\text{obs}} \gtrsim 10$ MeV. For this reason, in the following section we restrict our analysis to the lower range of γ_{max} values, i.e. $\gamma_{\text{max}} \approx 10^4 - 10^5$.

5.2 The multi-blob supercritical model

In the previous section we studied the characteristics of a photon outburst powered by HCS. We move next to apply these ideas to GRBs with light curves consisting of multiple spikes. To do so we construct synthetic light curves by allowing multiple blobs to be ejected in succession from a central source. Each one of them, depending on their initial conditions, could either enter the supercritical regime and produce one or multiple flares or could remain in the subcritical regime and show no flaring activity at all. The superposition of individual light curves produces light curves that have, as we show below, similarities to the GRB ones.

5.2.1 The relation between the spectral peak energy and the bolometric photon energy

Here we study how the energetics of our model compare with those of observed GRBs. We begin this analysis by assuming that a regular engine emits, every Δt_{off} , N expanding blobs, which have all, for the time being, the same initial set of parameters and are in the supercritical state. We also make the assumption that each blob produces a supercritical light curve that consists of a single flare. The total duration of the GRB emission is then:

$$T_{\text{tot}}^{\text{obs}} = N(\Delta t_{\text{off}}^{\text{obs}} + \Delta t_{1/2}^{\text{obs}}) \quad (17)$$

where $\Delta t_{1/2}^{\text{obs}}$ is the full width at half maximum of each single flare that is determined by the model parameters, i.e. r_{in} , B_{in} , u_{exp} , and Γ . We compute the emission for various parameter sets assuming a fixed $T_{\text{tot}}^{\text{obs}}$ (here, we set $T_{\text{tot}}^{\text{obs}} = 60$ s). This can be achieved by changing the number of blobs or the timescale between successive blob ejections from the central engine. For each parameter set we compute the emission from a single blob and record $\Delta t_{1/2}^{\text{obs}}$ and $\varepsilon_{\text{pk}}^{\text{obs}}$. We also

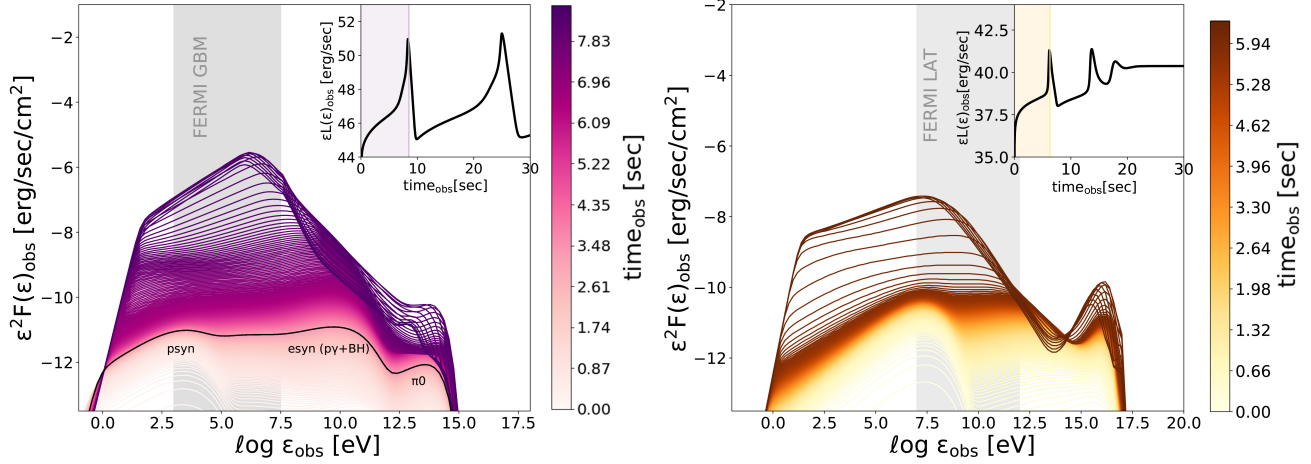


Figure 6. Left panel: A supercritical case chosen from the runs of Fig. 5 in the case where $\gamma_{\max} = 10^{4.5}$ (shown in the inset plot) and the corresponding photon spectra (shown in the main plots). The spectra correspond to the time period of the outburst’s rise. This time period is also shown in highlighted stripe in the inset plot. Each spectrum differs from the previous one $1 r_{\text{in}}/c$ and this is also shown in the colour bar. Right panel: Same as in the left panel for a supercritical case where $\gamma_{\max} = 10^{6.5}$ chosen from the runs of Fig. 5. In both cases we have not taken into account the photon attenuation by EBL for the spectra construction. The vertical grey regions depict the energy bands that the Fermi LAT and Fermi GBM observe. The above spectra are computed in the observer’s frame, assuming $\Gamma = 100$ and $z = 2$.

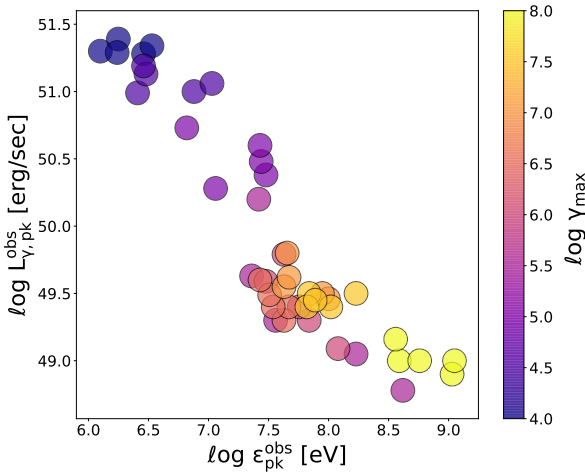


Figure 7. A plot of the photon luminosity at peak time of the first flare, $L_{\gamma,\text{pk}}^{\text{obs}}$, as a function of the photon energy that corresponds to the peak of the photon spectrum released at the same moment $\epsilon_{\text{pk}}^{\text{obs}}$. All the results are computed for different values of maximum proton Lorentz factor γ_{\max} , shown in colour. The parameters used are the same as in Fig. 6.

compute the bolometric photon energy $E_{\gamma,\text{tot}}^{\text{obs}}$ that is released during the outburst, following eq. 16. This is equivalent to the isotropic equivalent energy computed from the observed GRB fluence (e.g. Nava et al. 2008; Tu & Wang 2018).

GRBs are characterised by a number of correlations between different observational parameters. The Amati relation is a correlation between the GRB equivalent isotropic energy and its rest-frame peak energy $\epsilon_{\text{pk}}^{\text{obs}}$ (Amati, L. et al. 2002). Noting that the output parameter of our model $E_{\gamma,\text{tot}}^{\text{obs}}$ is equivalent to the isotropic energy entering the Amati relation we proceed with a rough comparison of the two.

In Fig. 8 we show the values of $\epsilon_{\text{pk}}^{\text{obs}}$ and $E_{\gamma,\text{tot}}^{\text{obs}}$ obtained by Minaev

& Pozanenko (2019) from a sample of 275 long GRBs. We overplot our results for a single blob (Case A) computed for a set of parameters from Fig. 5 ($B_{\text{in}} = 10^4$ G, $r_{\text{in}} = 10^{11}$ cm, $L_{\text{p,in}} = 10^{42.5}$ ergs $^{-1}$, $\gamma_{\max} = 10^4$, $u_{\text{exp}} = 10^{-2.5}c$). Our results depend on the choice of the bulk Lorentz factor as indicated in the figure by the different markers. For Case A specifically we find $\Delta t_{1/2}^{\text{obs}} = 0.8 \times (\frac{1+z}{3})(\frac{100}{\Gamma})$ s and $\epsilon_{\text{pk}}^{\text{obs}} = 10^3 \times (\frac{3}{1+z})(\frac{\Gamma}{100})$ keV (see teal markers). The solid teal line that connects the markers corresponds to intermediate bulk Lorentz factors. The light teal coloured region indicates the increase in the isotropic photon energy in case more identical blobs were emitted from the central engine. Assuming that $\Delta t_{1/2}^{\text{obs}} \approx \Delta t_{\text{off}}^{\text{obs}}$, we can estimate the maximum number of blobs which are emitted in order to observe a total light curve that lasts 60 s. For example, $E_{\gamma,\text{tot}}^{\text{obs}} \approx 2.4 \times 10^{53}$ erg would be produced, if the central engine was ejecting 37 identical blobs with $\Gamma = 100$ every 0.8 s.

We perform the same analysis by altering one of the blob parameters and compare the results. In Case B (see orange markers) we increase the initial radius of each expanding blob, i.e. $r_{\text{in}} = 3.16 \times 10^{11}$ cm. One needs higher proton luminosity, i.e. $L_{\text{p,in}} = 10^{42.9}$ erg s $^{-1}$ in order to recapture the supercritical flare. Each blob emits as a result a higher $E_{\gamma,\text{tot}}^{\text{obs}}$, having however a larger $\Delta t_{1/2}^{\text{obs}}$. If $\Gamma < 100$ then $\Delta t_{1/2}^{\text{obs}} > 4$ s, and the pulse of each blob is broad enough to create a FRED-like GRB light curve instead of a highly variable one.

Similar results are found when the expansion velocity is altered, i.e. $u_{\text{exp}} = 10^{-2}c$ (see magenta markers, Case C in Fig. 8). In this case $\epsilon_{\text{pk}}^{\text{obs}}$ is higher compared to that of Case A. This can be explained if one considers that a higher expansion velocity within the same time interval leads to a larger source, which is more optically thin, thus allowing the escape of higher energy photons.

5.2.2 Synthetic GRB spectra and light curves

In order to show that HSC produces highly variable light curves that do not depend on the randomness of the time intervals between successive blobs but on the inherent non-linearity of HSC itself, we

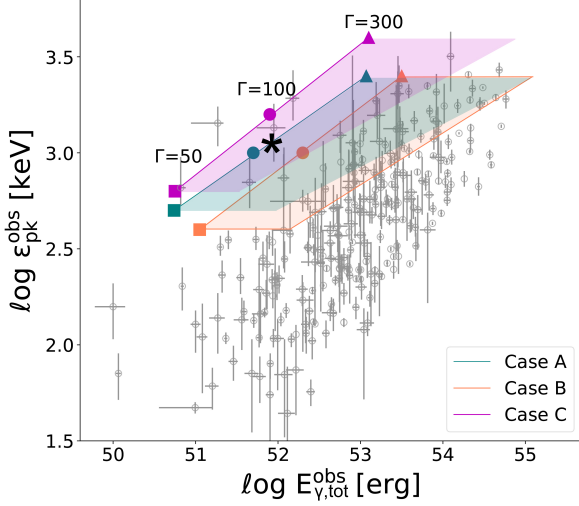


Figure 8. The Amati correlation for 275 long GRBs shown in [Minaev & Pozanenko \(2019\)](#) (empty grey circles). The coloured markers correspond to the values of $E_{\gamma,\text{tot}}^{\text{obs}} - \epsilon_{\text{pk}}^{\text{obs}}$ derived from our model in the case of one blob that emits a single supercritical flare. We present the results for three bulk Lorentz factors, $\Gamma = 300$ in triangles, $\Gamma = 100$ in circles and $\Gamma = 50$ in squares for three cases. In Case A, $B_{\text{in}} = 10^4$ G, $r_{\text{in}} = 10^{11}$ cm, $\gamma_{\text{max}} = 10^4$, $L_{\text{p,in}} = 10^{42.5}$ erg s $^{-1}$, $u_{\text{exp}} = 10^{-2.5}c$. For the other cases, all parameters are kept fixed except for: $r_{\text{in}} = 3.16 \times 10^{11}$ cm and $L_{\text{p,in}} = 10^{42.8}$ erg s $^{-1}$ (Case B) and $u_{\text{exp}} = 10^{-2}c$ and $L_{\text{p,in}} = 10^{42.9}$ erg s $^{-1}$ (Case C). The light coloured regions indicate how the results would change if multiple identical blobs were ejected from the central engine, producing a multi-pulse light curve. The black asterisk indicates the results of the next section in the case where $\Gamma = 100$.

produce synthetic GRB light curves as follows. We assume that the blobs are ejected periodically from the central engine with slightly different initial conditions, varying in a narrow range around a set of parameters that lead to HSC.

As an indicative example, we construct a synthetic light curve with $N = 10$ blobs of initial radius $r_{\text{in}} = 10^{11}$ cm. These are ejected from the central engine every $50 r_{\text{in}}/c$ (as measured in the comoving frame), which corresponds roughly to $\Delta t_{\text{off}}^{\text{obs}} = 5$ s in the observer’s frame, assuming that $z = 2$ and $\Gamma = 100$.

We assume that the initial magnetic field of the source (in logarithm) is following a Gaussian distribution with a median value at $\log(B_{\text{in,med}}) = 4.3$ G and a standard deviation $\log \sigma = 0.2$. We pick randomly its value for each blob (with a resolution of 0.1 in logarithmic scale)³. We also select values for $\log(\gamma_{\text{max}})$ from a Gaussian distribution, with median value $\log(\gamma_{\text{max,med}}) = 5$ and standard deviation of $\log \sigma = 0.2$. We also take into consideration that only small values of maximum proton Lorentz factors, i.e. $\gamma_{\text{max}} = 10^4 - 10^{5.5}$ yield photon spectra that peak approximately at 1 MeV (see Fig. 7). We calculate next the initial proton luminosity by assuming that it is proportional to the Poynting luminosity of the outflow, i.e. $L_{\text{p,in}} = \xi B_{\text{in}}^2 r_{\text{in}}^2 c$, where $\xi \geq 1$. Here, we choose $\xi = 60$. To be consistent with the findings of the previous section, we set $u_{\text{exp}} = 10^{-2.5}c$ and inject protons in each blob until $T_{\text{B}} = 400 r_{\text{in}}/c$;

³ An even higher resolution in the selection of $\log(B)$ would not change the resulting light curves and photon spectra.

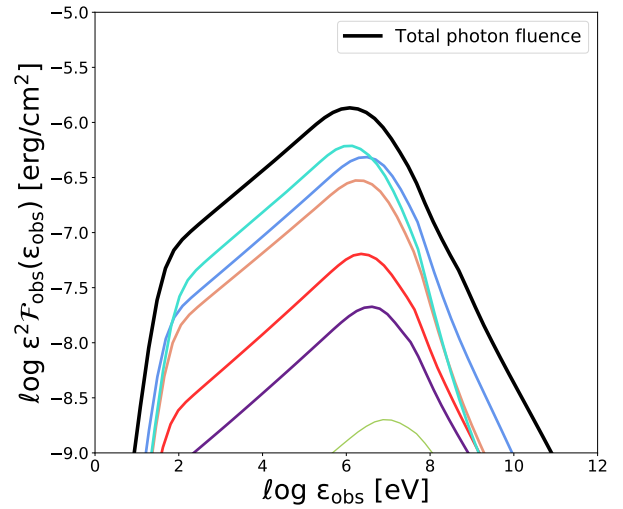
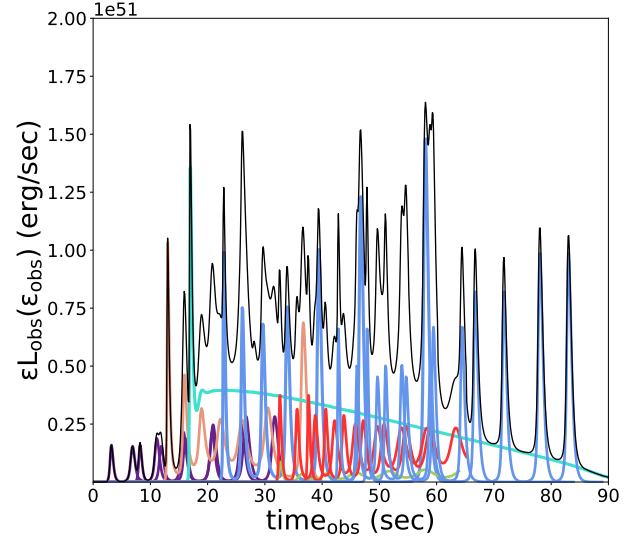


Figure 9. Upper panel: The light curve produced by the superposition of the emission of ten blobs showing supercritical behaviour (black solid line). The bulk Lorentz factor of the outflow is $\Gamma = 100$. Each coloured light curve shows the correspondence of each emitting blob (see also Table 1 for the exact blob parameters). Lower panel: The total fluence per photon energy (solid black line). The coloured lines correspond to the total spectra produced by each blob and are same coloured coded as the light curves of the upper plot.

within this time at least one supercritical flare manifests (see also Sec. 5.1). The model parameters are summarised in Table 1.

We numerically compute the bolometric electromagnetic signal from each blob. The superposition of light curves from individual blobs (coloured curves) yields the synthetic light curve, which is shown with solid black line in the upper panel of Fig. 9. The total flare produced is highly variable, lasts about 90 s, and the variability timescale, here defined as $\Delta t_{1/2}^{\text{obs}}$, ranges between 0.1 and 1.5 s. The radiative efficiency of the burst is $E_{\gamma,\text{tot}}^{\text{obs}}/E_{\text{p,tot}}^{\text{obs}} \approx 0.15$.

In the lower panel of Fig. 9 we show in colour the (differential in energy) fluence emitted by each blob, $\mathcal{F}_{\text{obs}}(\epsilon_{\text{obs}})$ [erg cm $^{-2}$ erg $^{-1}$]. We compute this by integrating the observed photon energy flux, $F_{\text{obs}}(\epsilon_{\text{obs}}, t_{\text{obs}}) = \Gamma^3 L_{\gamma}(\epsilon)/4\pi d_{\text{L}}^2$ over T_{B} . Here, d_{L} is the luminosity

Table 1. Parameters of 10 blobs used for the construction of a synthetic GRB-like light curve. Colours indicate the contribution of individual blobs to the overall light curve and spectra displayed in Figs. 9 and 10.

No. blobs	B_{in} (G)	$L_{\text{p,in}}$ (erg s^{-1})	γ_{max}	
1	5×10^3	1.3×10^{42}	7.9×10^5	Light Green
1	10^4	2.5×10^{42}	1.8×10^5	Purple
2	1.6×10^4	5×10^{42}	7.9×10^4	Red
3	2×10^4	7.9×10^{42}	10^5	Blue
2	3×10^4	1.25×10^{43}	2.2×10^4	Orange
1	5×10^4	2.5×10^{43}	1.4×10^4	Cyan

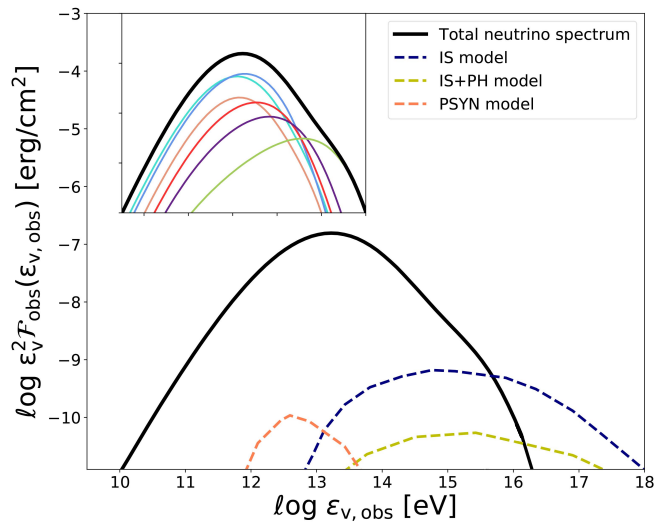


Figure 10. The all-flavour neutrino fluence (solid black line) calculated for a HSC burst with 10 expanding blobs. In the inset plot we show the neutrino fluence observed from each expanding blob, same colour coded as the photon spectra and light curves of Fig. 9. The dashed lines correspond to neutrino spectra computed with the internal shock (IS), the internal shock+photospheric dissipation (IS+PH) and the proton synchrotron (PSYN) models, as shown in Pitik et al. (2021).

distance of the GRB. The spectra are colour coded in the same way as the light curves of the upper panel (see also Table 1). The black solid line is the superposition of the individual photon fluences. The total spectrum peaks at approximately $\varepsilon_{\text{pk}}^{\text{obs}} = 1$ MeV, which is typical for the GRB prompt emission. The blob with the highest value of γ_{max} (see light green curve) emits photon spectra that peak at 10 MeV. However it does not contribute drastically to the total photon spectrum or to the total light curve because of the low value of $L_{\text{p,in}}$. On the other hand, the emission from the blob with the highest value of $L_{\text{p,in}}$ and lowest value of γ_{max} (see cyan curve) is imprinted on the total light curve and the peak of the photon spectrum. Furthermore, the blue light curve, which is the most variable of all, corresponds to the emission of three identical blobs. Even though their $L_{\text{p,in}}$ is lower than that of the cyan curve case, the superposition of their fluences has a similar effect on the total spectrum. Overall the observed isotropic photon energy of this burst is $E_{\gamma,\text{PH}}^{\text{obs}} \approx 10^{52}$ erg (2.5×10^{53} erg) for $\Gamma = 100$ (300), which places it in the upper part of the $\varepsilon_{\text{pk}}^{\text{obs}} - E_{\gamma,\text{tot}}^{\text{obs}}$ diagram (see the black asterisk in Fig. 8 for the case of $\Gamma = 100$). The results are compatible with a typical long GRB.

5.2.3 The total neutrino fluence

High-energy neutrinos are a guaranteed by-product of the HSC model (see also Petropoulou et al. 2014). It is therefore interesting to compare the neutrino predictions of our model with other existing ones. In order to compute the all-flavour neutrino spectra emitted by each expanding blob, we utilise the Dimitrakoudis et al. (2012) numerical code that treats in detail neutrino emissivities using the event generator SOPHIA (Mücke et al. 2000). Coloured curves in Fig. 10 show the contribution from individual blobs to the total neutrino fluence (black line). Here, the same colour coding as in Fig. 9 is used. The total neutrino emission of the burst peaks at ≈ 10 TeV and is dominated mostly by the cyan and blue spectra. The cyan spectrum, in particular, which corresponds to the blob with the lowest γ_{max} -highest $L_{\text{p,in}}$ values, controls the total peak energy and fluence. On the other hand the green spectrum, which correspond to the blob with the highest γ_{max} -lowest $L_{\text{p,in}}$ values, contributes mostly to the highest part of the neutrino spectrum energies. The ratio of the peaks of the total photon to all-flavour neutrino fluences in this example case is approximately $\mathcal{F}_{\gamma,\text{pk}}^{\text{obs}}/\mathcal{F}_{\nu,\text{pk}}^{\text{obs}} \approx 12.5$.

In Fig. 10 we also show the predicted neutrino spectra shown in Pitik et al. (2021), who computed the neutrino production for a benchmark high-luminosity GRB, among others in the internal shock model (IS, Rees & Meszaros 1994), in the internal shock model with dissipative photosphere (IS+PH, Toma et al. 2011) and in the proton synchrotron marginally fast cooling model (PSYN, Florou et al. 2021; Pitik et al. 2021). Because these models were computed for a GRB with a different γ -ray fluence than ours, we appropriately rescaled the neutrino fluence spectra of Pitik et al. (2021) for a fair comparison to our results. These models are overplotted with dashed dark blue, yellow and orange curves respectively. The neutrino spectrum of the HSC model is about two orders of magnitude higher than the expected neutrino spectrum of the IS model, and peaks at about two orders of magnitude lower energy. The lower peak energy and higher fluence found in the HSC model compared to the IS scenarios are a direct consequence of the fact that the HSC model for GRBs requires relatively low energies of γ_{max} (see Sec. 4) and is characterised by high neutrino production efficiency (see e.g. Petropoulou et al. 2014). The low values of γ_{max} that are needed to explain the MeV photon spectrum with proton synchrotron radiation in the PSYN scenario lead to similar peak neutrino energies to the HSC model. Meanwhile, the neutrino production efficiency in the PSYN scenario is much lower than in the HSC model, since protons are cooling via synchrotron radiation in the presence of very strong magnetic fields in the former case.

6 SUMMARY & DISCUSSION

In this paper we have extended recent work on HSC by examining its *modus operandi* in expanding sources. Prompted by our results we have applied them to the GRB prompt emission. We summarize next our basic results and discuss some aspects of our model.

HSC is a universal property of relativistic proton plasmas and appears *spontaneously* once appropriate conditions are satisfied. Its physical premise is based on a gradual proton accumulation inside the source and a sudden dissipation of the stored energy via one or more photon outbursts, bearing similarities to nuclear piles. These outbursts are, therefore, a *natural* consequence of the phase transition that the hadronic plasma undergoes and appear even when all parameters are kept constant.

HSC can occur only for specific combinations of initial radii,

Table 2. A summary of the results in this section which are compatible with the GRB phenomenology. The symbol \uparrow indicates increase, while the symbol \downarrow indicates decrease. Furthermore we sign with \checkmark the parameters that agree with the GRB phenomenology and with \times those that do not agree. We denote the multiple bursts with MB and the single burst with SB.

Parameters	Modification	Results		
		Light curves (LC)	Photon Spectra (SED)	Relevance to GRBs
u_{exp}/c	$u_{\text{exp}} \uparrow$	MB \rightarrow SB ,	$\epsilon_{\text{pk}}^{\text{obs}} \uparrow$	LC \checkmark , SED \times
$B \sim r^{-q}$	$q \uparrow$	MB \downarrow	$\epsilon_{\text{pk}}^{\text{obs}} \approx \text{constant}$	LC \checkmark , SED \checkmark
γ_{max}	$\gamma_{\text{max}} \uparrow$	MB \rightarrow SB \rightarrow MB	$\epsilon_{\text{pk}}^{\text{obs}} \uparrow$	LC \checkmark , SED \times

magnetic fields and proton energies. Other parameters like the power-law indices of the magnetic field and proton luminosity radial profiles as well as the power-law slope of the proton energy distribution play only an auxiliary role, as they do not qualitatively change the general picture described above. Determination of the critical conditions leading to HSC is still not sufficient for fully understanding the problem under study. The non-linear stages of HSC require a fully numerical treatment of the physical processes coupling photons with relativistic protons. Due to the complexity of the problem, there are only empirical ways of mapping the initial critical conditions to the final outcome. These involve a plethora of temporal and spectral signatures that can be tested readily against observations.

The role of adiabatic expansion to the manifestation of HSC has not been explored so far. We therefore studied thoroughly the effects of the adiabatic expansion velocity on the phenomenology of HSC. Small expansion velocities favour short-duration spiky outbursts characterised by high radiative efficiency. As the expansion velocity becomes larger, the bursts appear longer, smoother and less efficient. Also the multiplicity of bursts decreases with increasing expansion velocity, degenerating into a single burst when $u_{\text{exp}} \gtrsim 0.01c$. Single bursts can still be produced up to very high expansion velocities $\sim 0.5c$ (see e.g. Fig. 3). In other words, HSC persists for all expansion velocities, a fact that is impressive by itself if one considers that its onset depends on the proton column density. It is exactly because of this dependence, that higher initial proton luminosities are needed as u_{exp} becomes larger. Mastichiadis et al. (2020) showed that the energy density in relativistic protons U_p greatly exceeds the energy density in magnetic fields U_B for stationary sources in HSC. This result also holds for expanding sources where both energy densities vary continuously. Systems where $U_B \approx U_p$ never become supercritical. Furthermore, although the choice of a steeper magnetic field profile, e.g. $1/r^2$, for fixed initial proton luminosities and expansion velocities, makes the system more luminosity demanding, overall it leads to similar results as the flatter case of $1/r$.

The above epitomise some of the key results of HSC in expanding sources in the absence of external radiation fields and injection of relativistic (primary) electrons in the source. Both aspects have been shown to have a stabilising effect on the non-linear development of HSC in stationary sources (Mastichiadis et al. 2020), which also apply to expanding systems. For instance, the system reaches quickly (within a few source light-crossing times) a steady state characterised by high radiative efficiency without exhibiting bursty behaviour, if the injection luminosity of primary electrons exceeds $\sim 10\%$ of the proton luminosity. Similarly, if the density of external radiation fields is higher than the intrinsic photon density, then the non-linear coupling between protons and their own radiation is weakened. In light of these results we continue our discussion on the relevance of HSC to the GRB prompt emission.

We find that emitting regions (blobs) with initial radii $\sim 10^{11} - 10^{12}$ cm and maximum proton Lorentz factors $\sim 10^4 - 10^5$ produce outbursts with characteristics that are similar to those observed from

GRBs during the prompt phase. For small expansion velocities the light curves consist of multiple spikes with typical duration of a few tenths of the second and spectra that peak at $\sim \text{MeV}$ energies. Both features are consistent with the GRB phenomenology. As explained earlier, there is no *a-priori* reason that this should be the case. Interestingly, the expansion velocity also controls the appearance of the light curve, as higher expansion velocities give rise to single-pulse outbursts that resemble FRED-like GRB light curves. Because the photon pulses from a single slowly expanding blob are separated by a few hundreds source light-crossing times, one needs to superimpose the emission of a few blobs to obtain multi-pulse light curves, as those observed in many GRBs. Even small variations in the initial conditions between successive blobs can produce highly variable light curves (see Table 1 and Fig. 9).

The expansion velocity also affects the peak energy of the photon spectrum, $\epsilon_{\text{pk}}^{\text{obs}}$. Faster expansion of the source roughly corresponds to a lower intrinsic opacity to $\gamma\gamma$ pair production, thus pushing $\epsilon_{\text{pk}}^{\text{obs}}$ beyond the MeV range for all other parameters kept fixed (see Fig. 8). Another way to obtain photon spectra peaking in the GeV range with our model is to consider the injection of protons with higher maximum energies (see Figs. 6). The prediction of the HSC model is that if such GRBs do exist, they should be on average less luminous than their MeV counterparts, as illustrated in Fig. 7. The maximum proton energy also affects the appearance of the light curve, with multi-pulse light curves produced from a single blob containing protons with $\gamma_{\text{max}} \approx 10^4 - 10^5$ or $\gtrsim 10^{6.5}$. For intermediate values, the outbursts usually consist of a single pulse. Nonetheless, the HSC model cannot explain GRBs with soft spectra peaking in the 10–100 keV range.

Some of the above results are summarised in Table 2, where we show the dependence of the supercritical temporal and spectral behaviour on the expansion velocity, the magnetic field profile and the maximum Lorentz factor. We note with \uparrow (\downarrow) the parameter increase (decrease). We also compare our results with the GRB phenomenology, denoting with \checkmark the cases where the light curves and the photon spectra bear broad similarities with the observations.

Since the photon spectrum at the peak time of the outburst is a result of intense electromagnetic cascades from secondary pairs and γ -ray photons, we expect that TeV photons will be severely attenuated inside the source and the ratios of spectral luminosities between TeV and MeV can be as low as $\sim 10^{-5}$ (see e.g. Fig. 6). TeV photons will also be attenuated en route to us by the photons of the extragalactic background light (EBL). Therefore, the HSC model suggests that detection of prompt GRB emission at TeV energies would be challenging even for sensitive instruments such as the Cherenkov Telescope Array (CTA, Knödlseeder 2020). For example, the average photon spectrum of the indicative burst shown in Fig. 9 (lower panel) exceeds the 50 hr CTA sensitivity curve at 1 TeV only for $z \lesssim 0.3$ (assuming the EBL model of Finke et al. (2010)).

Besides electromagnetic radiation high energy neutrinos are copiously produced in HSC outbursts. For those in particular that

are powered by protons of relatively low energies (e.g. $\gamma_{\max} = 10^4 - 10^5$), we find that the all-flavour neutrino spectrum peaks at ~ 10 TeV ($3/(1+z)$) and has a peak fluence of about 10% of the peak photon energy fluence (see lower panel in Fig. 9 and 10). The neutrino-to-photon peak fluence ratio can range between 3% and 30% depending on the main model parameters, like u_{exp} , γ_{\max} and B . This ratio however cannot be fully determined *a priori* by simply selecting the appropriate initial conditions, as it is the outcome of the proton-photon interactions in the non-linear stages of HSC. As a result, the neutrino predictions of the HSC model for GRBs are substantially different than those typically found in the literature (Gao et al. 2012; Baerwald et al. 2015; Mészáros 2015; Bustamante et al. 2017; Biehl et al. 2018; Pitik et al. 2021; Florou et al. 2021).

We can also compare the predictions of the HSC model with the stacking flux limits from the IceCube neutrino telescope. To estimate the all-sky quasi-diffuse flux of muon neutrinos and antineutrinos we assume that our benchmark long-duration GRB at $z = 2$ with $E_{\gamma, \text{tot}}^{\text{obs}} \simeq 10^{52}$ erg s $^{-1}$ and $\Gamma = 100$ (see Sec. 5.2.2) is representative of the entire GRB population. Given a rate of long GRBs $\dot{N} = 667$ yr $^{-1}$ (Aartsen et al. 2017), the stacking flux for muon neutrinos over the whole sky can be written as $\Phi_{\nu_{\mu} + \bar{\nu}_{\mu}} \simeq (\dot{N}/4\pi)(\mathcal{F}_{\nu + \bar{\nu}}/3)$, where we assumed vacuum flavour mixing. Using $\mathcal{F}_{\nu + \bar{\nu}} \simeq 10^{-7}$ erg cm $^{-2}$ as a conservative value (i.e. 10% of the γ -ray fluence), we find $\Phi_{\nu_{\mu} + \bar{\nu}_{\mu}} \simeq 3.7 \times 10^{-11}$ GeV cm $^{-2}$ s $^{-1}$ sr $^{-1}$. With a peak energy around 10 TeV our prediction is well below the IceCube stacking limit (Aartsen et al. 2017) in agreement with the non-detection of high-energy neutrinos from targeted GRB searches. It is however very close to the projected limit for IceCube-Gen2 in the energy range of 10–100 TeV (Aartsen et al. 2021b), suggesting that the HSC scenario could be testable within the next decade with neutrino observations.

ACKNOWLEDGEMENTS

IF acknowledges that this research is co-financed by Greece and the European Union (European Social Fund- ESF) through the Operational Programme «Human Resources Development, Education and Lifelong Learning» in the context of the project “Strengthening Human Resources Research Potential via Doctorate Research – 2nd Cycle” (MIS-5000432), implemented by the State Scholarships Foundation (IKY). MP and IF acknowledge support from the MERAC Foundation through the project THRILL.

DATA AVAILABILITY

The data shown in Fig. 8 are adopted from Minaev & Pozanenko (2019). All numerical models presented in this paper were computed using a proprietary numerical code. They can be shared upon reasonable request to the authors.

REFERENCES

- Aartsen M. G., et al., 2017, *ApJ*, **843**, 112
- Aartsen M. G., et al., 2021a, *Journal of Physics G: Nuclear and Particle Physics*, **48**, 060501
- Aartsen M. G., et al., 2021b, *Journal of Physics G Nuclear Physics*, **48**, 060501
- Abdalla H., et al., 2019, *Nature*, **575**, 464–467
- Abdo A. A., et al., 2009, *ApJ*, **706**, L138
- Ackermann M., et al., 2011, *The Astrophysical Journal*, **729**, 114
- Amati, L. et al., 2002, *A&A*, **390**, 81
- Asano K., Inoue S., 2007, *ApJ*, **671**, 645
- Asano K., Guiriec S., Mészáros P., 2009, *The Astrophysical Journal*, **705**, L191
- Baerwald P., Bustamante M., Winter W., 2015, *Astroparticle Physics*, **62**, 66
- Band D., et al., 1993, *ApJ*, **413**, 281
- Beloborodov A. M., Mészáros P., 2017, *Space Science Reviews*, **207**, 87–110
- Biehl D., Boncioli D., Lunardini C., Winter W., 2018, *Scientific Reports*, **8**
- Boula S., Mastichiadis A., 2022, *A&A*, **657**, A20
- Burgess J. M., Bégué D., Greiner J., Giannios D., Bacelj A., Berlato F., 2020, *Nature Astronomy*, **4**, 174
- Bustamante M., Heinze J., Murase K., Winter W., 2017, *The Astrophysical Journal*, **837**, 33
- Crider A., et al., 1997, *The Astrophysical Journal*, **479**, L39
- Dermer C. D., Atayan A., 2003, *Phys. Rev. Lett.*, **91**, 071102
- Dermer C. D., Atayan A., 2006, *New Journal of Physics*, **8**, 122
- Dimitrakoudis Mastichiadis, A. Protheroe, R. J. Reimer, A. 2012, *A&A*, **546**, A120
- Finke J. D., Razzaque S., Dermer C. D., 2010, *The Astrophysical Journal*, **712**, 238–249
- Florou I., Petropoulou M., Mastichiadis A., 2021, *Monthly Notices of the Royal Astronomical Society*, **505**, 1367
- Gao S., Asano K., Mészáros P., 2012, *Journal of Cosmology and Astroparticle Physics*, **2012**, 058
- Gendre B., et al., 2013, *The Astrophysical Journal*, **766**, 30
- Ghisellini et al., 2020, *A&A*, **636**, A82
- Goldstein A., et al., 2012, *The Astrophysical Journal Supplement Series*, **199**, 19
- Guiriec S., 2012, in 39th COSPAR Scientific Assembly. p. 682
- Hinshaw G., et al., 2013, *The Astrophysical Journal Supplement Series*, **208**, 19
- Kardashev N. S., 1962, *Azh*, **39**, 393
- Katz J. I., 1994, *ApJ*, **432**, L107
- Kazanas D., Georganopoulos M., Mastichiadis A., 2002, *ApJ*, **578**, L15
- Kirk J. G., Mastichiadis A., 1992, *Nature*, **360**, 135
- Knödseder J., 2020, The Cherenkov Telescope Array ([arXiv:2004.09213](https://arxiv.org/abs/2004.09213))
- Kumar P., Zhang B., 2015, *Physics Reports*, **561**, 1
- MAGIC Collaboration et al., 2019, *Nature*, **575**, 455
- Mastichiadis A., Kazanas D., Mar 2009, *ApJ*
- Mastichiadis A., Kirk J. G., 1995, *A&A*, **295**, 613
- Mastichiadis A., Kirk J. G., 1997, *A&A*, **320**, 19
- Mastichiadis A., Florou I., Kefala E., Boula S. S., Petropoulou M., 2020, *Monthly Notices of the Royal Astronomical Society*, **495**, 2458–2474
- Mészáros P., Rees M. J., Papathanassiou H., 1994, *The Astrophysical Journal*, **432**, 181
- Minaev P. Y., Pozanenko A. S., 2019, *Monthly Notices of the Royal Astronomical Society*, **492**, 1919–1936
- Murase K., 2008, *Phys. Rev. D*, **78**, 101302
- Murase K., Ioka K., Nagataki S., Nakamura T., 2008, *Phys. Rev. D*, **78**, 023005
- Mészáros P., 2015, Gamma Ray Bursts as Neutrino Sources, [doi:10.48550/ARXIV.1511.01396](https://arxiv.org/abs/1511.01396), <https://arxiv.org/abs/1511.01396>
- Mücke A., Engel R., Rachen J., Protheroe R., Stanev T., 2000, *Computer Physics Communications*, **124**, 290–314
- Nava L., Ghirlanda G., Ghisellini G., Firmani C., 2008, *Monthly Notices of the Royal Astronomical Society*, **391**, 639
- Oganesyan G., Nava L., Ghirlanda G., Celotti A., 2017, *ApJ*, **846**, 137
- Oganesyan G., Nava L., Ghirlanda G., Melandri A., Celotti A., 2019, *A&A*, **628**, A59
- Petropoulou M., Mastichiadis A., 2012, *MNRAS*, **421**, 2325
- Petropoulou M., Mastichiadis A., 2018, *Monthly Notices of the Royal Astronomical Society*, **477**, 2917
- Petropoulou M., Dimitrakoudis S., Mastichiadis A., Giannios D., 2014, *MNRAS*, **444**, 2186
- Pitik T., Tamborra I., Petropoulou M., 2021, *Journal of Cosmology and Astroparticle Physics*, **2021**, 034
- Preece R. D., Briggs M. S., Mallozzi R. S., Pendleton G. N., Paciesas W. S., Band D. L., 1998, *ApJ*, **506**, L23
- Racusin J. L., et al., 2008, *Nature*, **455**, 183
- Razzaque S., 2010, *The Open Astronomy Journal*, **3**, 150–155

- Rees M. J., Meszaros P., 1994, *The Astrophysical Journal*, 430, L93
- Sari R., Narayan R., Piran T., 1996, *ApJ*, 473, 204
- Sari R., Piran T., Narayan R., 1998, *The Astrophysical Journal*, 497, L17
- Schnabel J., Gal T., Aly Z., 2021, The KM3NeT Open Science System ([arXiv:2101.06751](https://arxiv.org/abs/2101.06751))
- Toma K., Wu X.-F., Mészáros P., 2011, *Monthly Notices of the Royal Astronomical Society*, 415, 1663
- Totani T., 1998, *The Astrophysical Journal*, 509, L81
- Tu Z. L., Wang F. Y., 2018, *The Astrophysical Journal*, 869, L23
- Vietri M., 1995, *The Astrophysical Journal*, 453, 883
- Vietri M., 1997, *Phys. Rev. Lett.*, 78, 4328
- Waxman E., 1995, *The Astrophysical Journal*, 452
- Waxman E., Bahcall J., 1997, *Phys. Rev. Lett.*, 78, 2292

This paper has been typeset from a \TeX/L\AA\TeX file prepared by the author.